nature methods

BRIEF COMMUNICATION

https://doi.org/10.1038/s41592-019-0592-7

Optogenetic activation of intracellular antibodies for direct modulation of endogenous proteins

Daseuli Yu[1], Hansol Lee[1], Jongryul Hong[1], Hyunjin Jung[1], YoungJu Jo[2,5], Byung-Ha Oh[1,3], Byung Ouk Park[4]* and Won Do Heo[1,3,4]*

Intracellular antibodies have become powerful tools for imaging, modulating and neutralizing endogenous target proteins. Here, we describe an optogenetically activated intracellular antibody (optobody) consisting of split antibody fragments and blue-light inducible heterodimerization domains. We expanded this optobody platform by generating several optobodies from previously developed intracellular antibodies, and demonstrated that photoactivation of gelsolin and β2-adrenergic receptor (β2AR) optobodies suppressed endogenous gelsolin activity and β2AR signaling, respectively.

Intracellular antibodies (intrabodies) have attracted interest for their ability to manipulate endogenous protein function[1,2]. Notably, small antibody fragments, such as single-domain antibodies (V_HH, known as nanobodies) and single-chain variable fragments (scFv), have been widely used as efficient tools to define the function of endogenous proteins and determine their roles in signaling pathways[3]. Despite the widespread use of intrabodies, no techniques for directly controlling intrabody activity in living cells have been reported. The current methods for inducing intrabody activity in cells rely on chemically induced intrabody expression[4] or degradation[5]. However, these methods do not allow for fine-tuned regulation of intrabody activity, limiting the use of intrabodies in dissecting complex signaling networks. Direct modulation of protein activity with an optogenetic tool adds further precision in terms of spatial and temporal regulation of proteins[6].

Here, we present an optogenetic platform for inducing activation of intrabodies that allows the function of endogenous target proteins to be precisely controlled in living cells. We combined a split-protein system and light-responsive proteins to generate an optogenetically activatable intracellular antibody (optobody).

To develop an optobody platform, we first identified the best-suited split site on opposite sides of complementarity-determining regions (CDRs) in a green fluorescent protein (GFP) nanobody[7], by conjugating each split GFP nanobody fragment to a FK506 binding protein fused to FKBP rapamycin binding protein (FKBP–FRB) (Fig. 1a and Supplementary Fig. 1a,b). The efficiency of each split site was measured by assessing the association of the corresponding split GFP nanobody with Mito-GFP (Supplementary Fig. 1c). We found that the split sites, which divide CDR1/2 and CDR3, produced clear accumulation of GFP nanobody fragments with Mito-GFP after rapamycin treatment, and that the N65/C66 split site was more efficient in rapamycin-mediated targeting of GFP (Fig. 1b and Supplementary Fig. 1d,e). The affinity of activated GFP nanobody N65/C66 fragments to GFP was analyzed by biolayer interferometry (BLI), which yielded an estimated affinity constant (K_D) value of 7.27×10^{-8} M, an affinity as high as that for the intact GFP nanobody (Fig. 1c,d and Supplementary Fig. 2). Therefore, the GFP nanobody fragments N65 and C66 were used in subsequent experiments. Although not the focus of this work, the chemogenetically activatable intracellular antibody (chemobody) may offer advantages for in vivo applications.

To create an optobody platform, we linked the GFP nanobody fragments N65 and C66 to the Magnet optical dimerization tools nMagHigh1 and pMagHigh1 (ref. [8]), respectively. The GFP nanobody N65-nMagHigh1 was paired with two different orientations of pMagHigh1 and GFP nanobody C66: pMagHigh1-C66 and C66-pMagHigh1 (Supplementary Fig. 3a). N65-nMagHigh1 paired with pMagHigh1-C66 showed efficient targeting to Mito-GFP in response to light stimulation (Supplementary Fig. 3b,c). Co-immunoprecipitation experiments supported the low background of the inactive GFP optobody in darkness and the light-induced capture of GFP by the activated GFP optobody (Supplementary Fig. 4). These results establish the N65/C66 split site and the indicated configuration of the Magnet fragments as the optimal optobody platform (Fig. 1e).

Separate GFP optobody fragments were accumulated at Mito-GFP immediately after light stimulation, reaching saturation after about 1 h (Fig. 1f,g, Supplementary Fig. 12a and Supplementary Video 1). The GFP optobody can specifically target GFP within the nucleus, at the plasma membrane, and on the cytoplasmic face of the Golgi apparatus (Supplementary Fig. 5a). The local stimulation in individual cells effectively activated the GFP optobody with high spatial resolution (Supplementary Fig. 5b and Supplementary Video 2). By varying the power density or duration of light input, we showed that a single pulse of light power greater than 100 μW mm^{-2} efficiently turned on the GFP optobody, whereas increasing the duration of light input at modest power density (50 μW mm^{-2}) induced higher-amplitude activation of the GFP optobody (Supplementary Fig. 5c,d).

The variable domain of the antibody contains a conserved disulfide bond that provides intrinsic stability[9]. The design of the optobody separates two cysteine residues (Cys24 and Cys94 on the GFP nanobody) from each other on the fragments before activation. A C24S mutant GFP optobody interacted less efficiently with Mito-GFP than the wild-type GFP optobody (Supplementary Fig. 6). This indicates that the interaction between two Cys residues may help activate and stabilize the optobody and restrict its flexibility for target binding.

[1]Department of Biological Sciences, Korea Advanced Institute of Science and Technology, Daejeon, Republic of Korea. [2]Department of Physics, Korea Advanced Institute of Science and Technology, Daejeon, Republic of Korea. [3]KAIST Institute for the BioCentury, Korea Advanced Institute of Science and Technology, Daejeon, Republic of Korea. [4]Center for Cognition and Sociality, Institute for Basic Science, Daejeon, Republic of Korea. [5]Present address: Department of Applied Physics, Stanford University, Stanford, CA, USA. *e-mail: bopark1@gmail.com; wondo@kaist.ac.kr

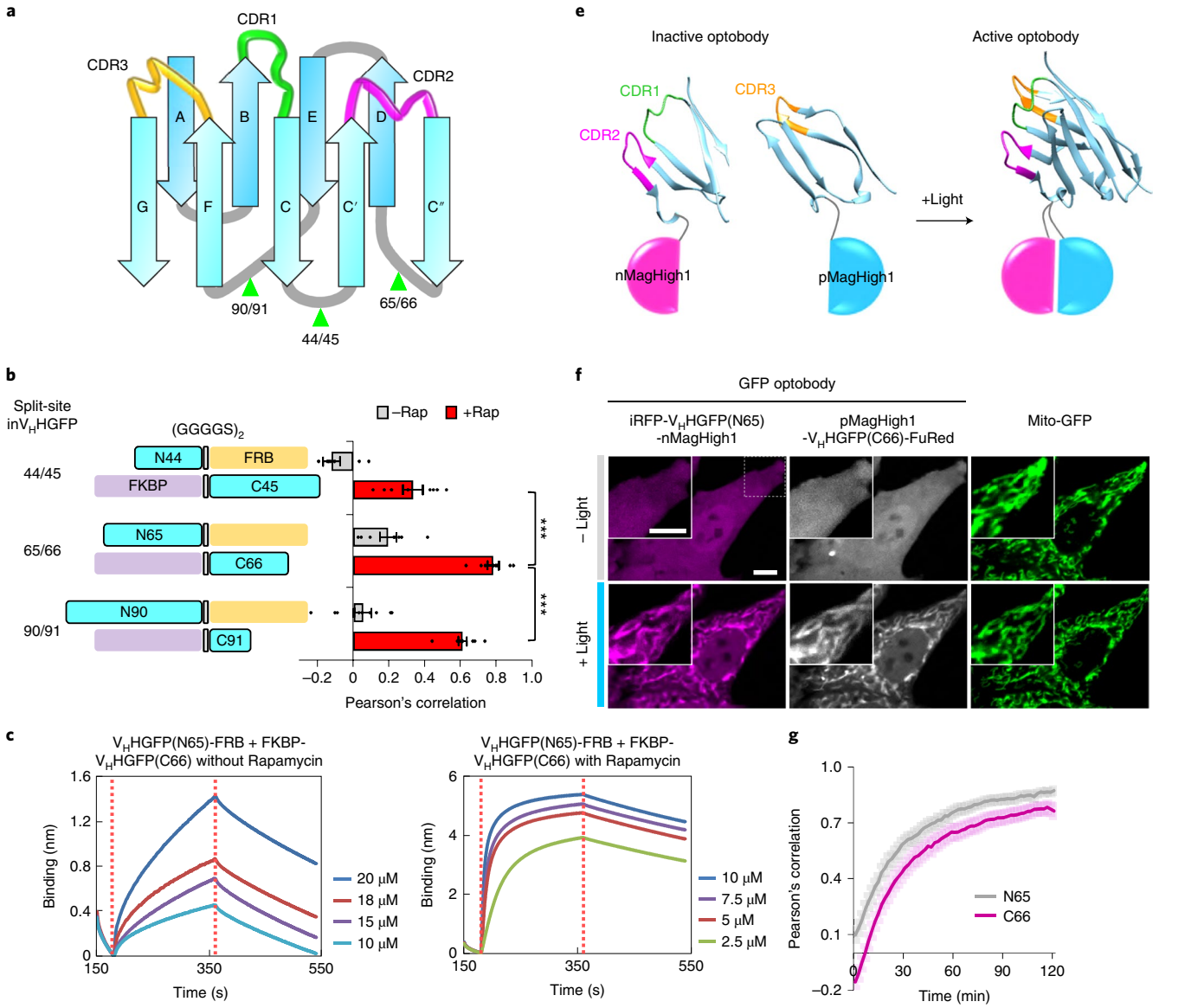

d

	K_{on} (10^4 Ms^{-1})	K_{off} (10^{-3} s^{-1})	K_D (M)
V_HHGFP	3.10 ± 0.06	1.72 ± 0.06	5.53×10^{-8}
$V_HHGFP(N65)$ + $V_HHGFP(C66)$ with Rapamycin	1.37 ± 0.03	1.00 ± 0.04	7.27×10^{-8}
$V_HHGFP(N65)$ + $V_HHGFP(C66)$ without Rapamycin	0.01 ± 0.63	5.48 ± 0.28	3.80×10^{-5}

Fig. 1 | Optobody design and development. a, Schematic representation of the secondary structure of a GFP nanobody and its split sites (indicated by green arrowheads). **b**, Three pairs of split GFP nanobodies fused to FRB and FKBP. Pearson's correlation for each split GFP nanobody with Mito-GFP in HeLa cells 4 h after addition of 500 nM rapamycin (rap; $n \geq 8$ for each group). ***$P < 0.005$ by Student's two-tailed t-test. **c**, Binding of inactive or activated GFP nanobody fragments 3 mg ml^{-1} of His_6-tagged GFP bound Ni-NTA probe on a BLItz system. Red dotted lines mark the start of binding (left) and dissociation (right) phases. **d**, Table showing the calculated kinetics parameters. **e**, Schematic depiction of blue-light induced activation of an optobody. **f**, Fluorescence images of HeLa cells expressing a GFP optobody N-terminal fragment, GFP optobody C-terminal fragment and Mito-GFP, before and 1 h after illumination with 488-nm light every 2 min. Scale bars, 10 μm. **g**, Pearson's correlation for each GFP optobody fragment with Mito-GFP in HeLa cells, tested as in **f**. Correlations were calculated for single cells ($n = 27$). Values are means ± s.e.m. Detailed statistical information is provided in the Methods.

To explore whether the optobody platform could be combined with other blue-light mediated photoreceptors, we replaced pMagHigh1 with pMag or pMagFast1 (ref. [8]) and generated a GFP optobody using iLID and SspB R73Q[10]. Contrary to our expectations, pMag- and pMagFast1-conjugated GFP optobodies are less efficiently activated by light stimulation, whereas a GFP optobody

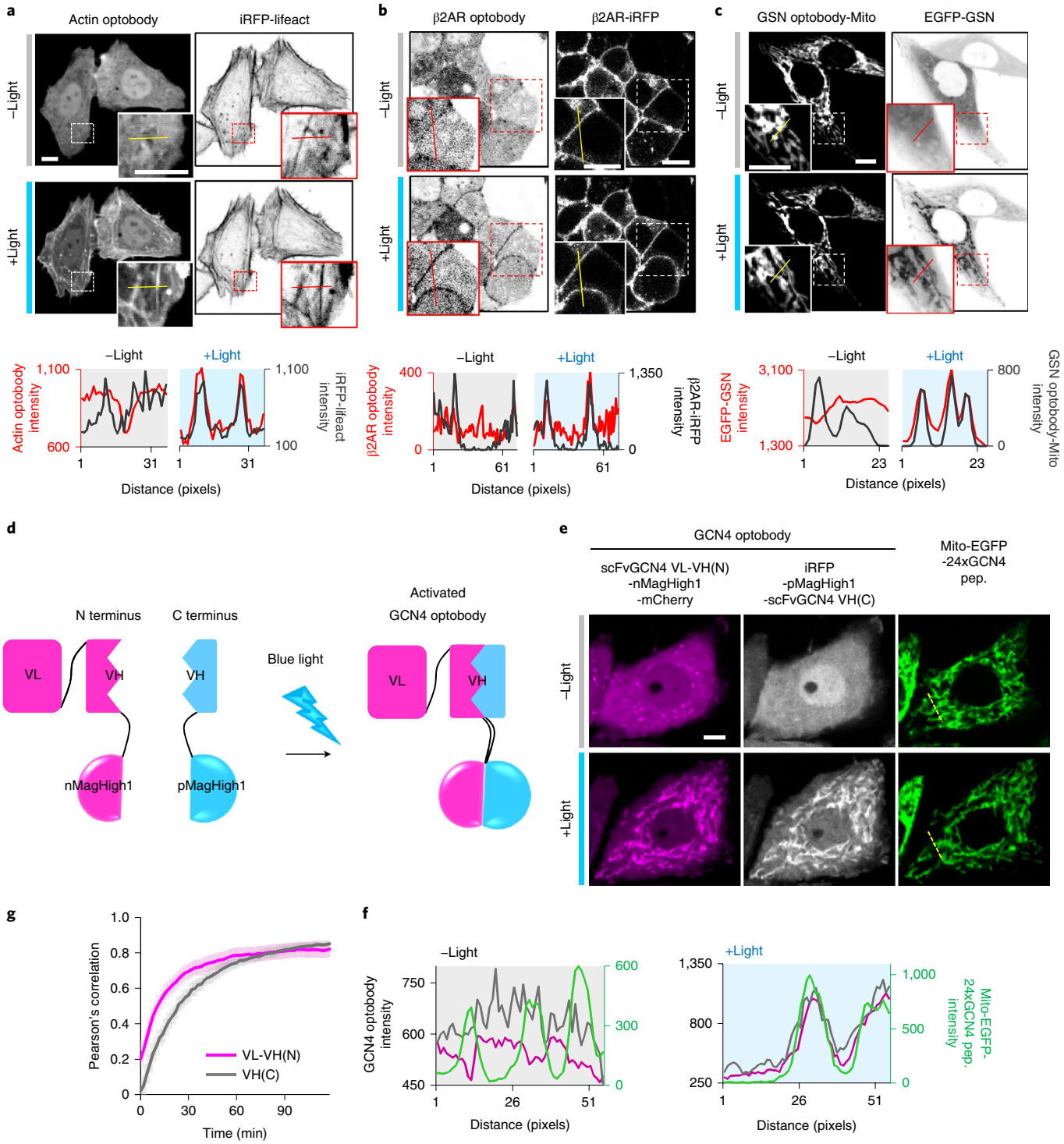

Fig. 2 | Applications of optobodies for inducible protein targeting and manipulation. a–c, Fluorescence images showing light-dependent operation of an actin optobody (**a**), β2AR optobody (**b**) and GSN optobody-Mito (**c**). Cells were stimulated with 488-nm (blue) light every 2 min for 1 h. Lower panels are optobody intensity profiles along the yellow and red lines in the upper images. **d**, Schematic depiction of an optobody derived from scFv. **e**, Images of HeLa cells expressing split-scFvGCN4 fragments (based on a split site in the VH domain) and Mito-EGFP-24xGCN4 peptide. Cells were illuminated every 2 min for 1 h. **f**, Intensity profile of a GCN4 optobody along the yellow lines on images **e**. **g**, Pearson's correlation for each GCN4 optobody fragment targeting the Mito-EGFP-24xGCN4 peptide following blue-light stimulation, obtained every 2 min ($n = 10$). Values are means ± s.e.m. Scale bars, 10 μm. Detailed statistical information is provided in the Methods.

fused to iLID and SspB R73Q was optogenetically activated as efficiently as nMagHigh1 and pMagHigh1 fused to the GFP optobody (Supplementary Fig. 7). These results suggest that optogenetic modules with a dimerization affinity comparable to that of nMagHigh1-pMagHigh1 or iLID-SspB R73Q are capable of forming an operational optobody.

Through switching off the light on the cells activating GFP optobody, we found no dissociation of GFP optobody from

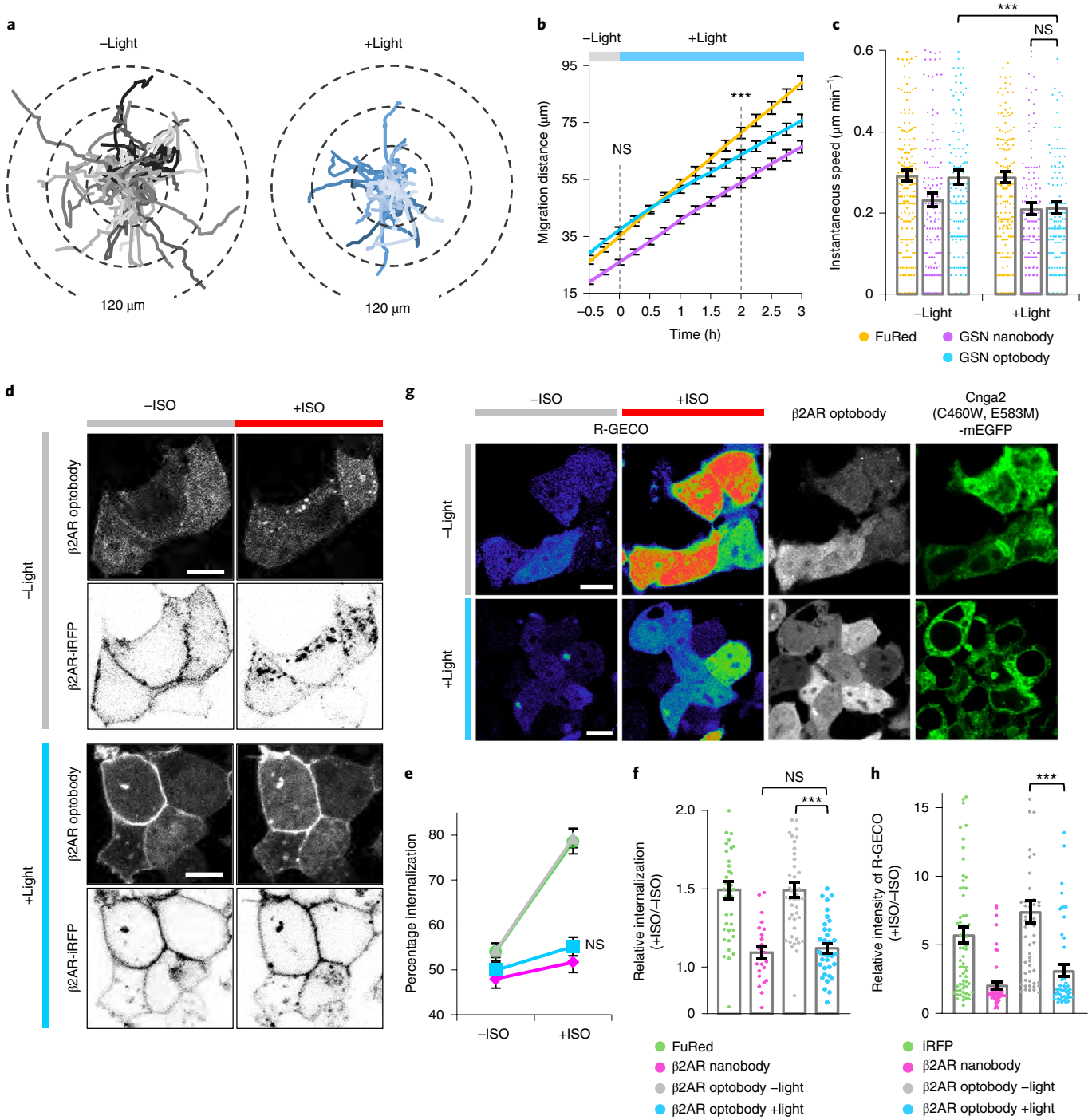

Fig. 3 | Optogenetic inhibition of endogenous GSN activity and β2AR signaling with a GSN optobody and β2AR optobody, respectively. a, Tracking the migration of a group of NIH3T3 cells expressing a GSN optobody, with and without light stimulation. Each line represents the migration path of one cell ($n = 50$), monitored every 3 min for 5 h with simultaneous blue-light illumination. **b**,**c**, Quantification of migration distance (**b**) and instantaneous speed (**c**) of NIH3T3 cells expressing FuRed, GSN nanobody and GSN optobody, and stimulated with light. Instantaneous speed at 0 h (−Light) and 2 h (+Light) points in **b** were measured ($n \geq 132$ for each group). **d**, Representative images of HEK293 cells expressing a β2AR optobody and β2AR-iRFP. Cells were illuminated with blue light every 3 min for 8 h and then treated with 1 μM ISO for 1 h. **e**,**f**, Quantification of β2AR-iRFP internalization in HEK293 cells expressing FuRed, β2AR nanobody or β2AR optobody, with or without light stimulation, 1 h after addition of 1 μM ISO addition ($n \geq 23$ for each group). **g**, Pseudocolor images of R-GECO and fluorescence images of β2AR optobody and Cnga2 (C460W, E583M)-mEGFP in HEK293 cells. Cells were illuminated as in **d** and treated with 1 μM ISO. **h**, Relative intensity of R-GECO before and after addition of 1 μM ISO in HEK293 cells expressing iRFP, β2AR nanobody or β2AR optobody with or without light stimulation ($n \geq 50$ for each group). Scale bars, 10 μm. Values are means ± s.e.m. NS, not significant, $^{***}P < 0.005$ by Student's two-tailed *t*-test. Detailed statistical information is provided in the Methods.

mitochondria-conjugated GFP (Supplementary Fig. 7e and Supplementary Video 3). To investigate how the activated GFP optobody maintains stable targeting of GFP even in darkness, we monitored detachment of the C-terminal fragment from the mito-conjugated N-terminal fragment in the absence or presence of GFP. As shown in Supplementary Fig. 8, GFP optobody fragments clearly

dissociated in the absence of GFP, but this dissociation was blocked by the presence of GFP. These results demonstrate that optobody activation is irreversible because of the high-affinity binding of the GFP optobody to GFP.

We next sought to convert the deGraFP[11] to a photo-inducible system; we replaced the NSlmb-GFP nanobody with NSlmb-GFP optobody. Following light-induced activation of the NSlmb-GFP optobody, EGFP-H2B intensity started to decrease, ultimately reaching a level comparable to that of the NSlmb-GFP nanobody (Supplementary Fig. 9). These results indicate the broad applicability of the optobody, showing that it simply converts a conventional method into a light-inducible system.

We also developed a mCherry optobody from a mCherry nanobody[12]. The mCherry optobody fragments showed no background of binding to Mito-mCherry in darkness, and were dramatically activated by blue-light stimulation, as shown for the GFP optobody (Supplementary Fig. 10). A mCherry optobody will be helpful for users with concerns about cross-talk between GFP and optogenetic tools used for optobody targeting of fluorescent proteins.

To expand the versatility of optobody to targeting of endogenous proteins, we generated an actin optobody, a β2AR optobody and a gelsolin (GSN) optobody, generated from nanobodies and a GCN4 optobody, generated from a scFv (Supplementary Fig. 11).

We first converted the actin nanobody[13] to an actin optobody. In darkness, the inactive actin optobody was dispersed in the cytosol of cells, but light stimulation induced activation of the actin optobody, resulting in its targeting to actin filaments (Fig. 2a, Supplementary Fig. 12b and Supplementary Video 4). Next, to generate a β2AR optobody, we engineered the nanobody, Nb60, which detects an inactive form of β2AR[14]. Light illumination triggered translocation of the activated β2AR optobody to the membrane, where it targeted inactive β2AR (Fig. 2b, Supplementary Fig. 12c and Supplementary Video 5). We then used a GSN nanobody (GSN Nb11) as a template for a GSN optobody, which specifically recognizes the GSN G2 domain[15]. On light stimulation, the mito-conjugated GSN optobody was activated and EGFP-GSN clearly moved toward the mitochondria (Fig. 2c, Supplementary Fig. 12d and Supplementary Video 6). We further tested whether the split GSN nanobody fragments retained their specificity for the target protein after activation. Treatment with rapamycin to activate the split GSN nanobody did not induce translocation of the GSN G4–G6 domain; however, the GSN G1–G3 domain did bind to the activated split GSN nanobody (Supplementary Fig. 13). These results indicate that reassembled nanobody fragments retain a specificity of the original nanobody.

In addition to nanobodies, we applied the optobody platform to scFvGCN4 (ref. [16]). When Magnet-conjugated variable heavy (VH) and light (VL) chain domains were expressed together, they spontaneously reassembled and bound to Mito-fused 24xGCN4 peptides, even in darkness (Supplementary Fig. 14b,c). Thus, we generated two pairs of scFvGCN4 fragments by splitting each variable domain as described for generation of the optobody (Fig. 2d and Supplementary Fig. 14a). The split fragments of scFvGCN4 VH domain accumulated at mitochondria on light stimulation (Fig. 2e–g, Supplementary Fig. 12e and Supplementary Video 7), whereas the split fragments of scFvGCN4 VL domain showed no targeting of mitochondria (Supplementary Fig. 14d,e). These results demonstrate that the activity of scFvGCN4 can also be adapted to the optobody system, but only the VH domain of scFv is suitable for this purpose.

We next assessed the suitability of GSN and β2AR optobodies as new tools for optogenetic inhibition on their endogenous target proteins. To investigate light-induced perturbation of GSN function by GSN optobody, we monitored migration of NIH3T3 cells expressing a GSN optobody, with or without light stimulation. Cells illuminated with blue light explored a more restricted territory than cells in darkness, exhibiting a considerable decrease in migration distance and instantaneous speed (Fig. 3a–c). Chemical-induced activation of split GSN nanobody fragments also led to inhibitory effects on cell movement (Supplementary Fig. 15). Spatiotemporal activation of GSN optobody recruited GSN protein at the subcellular level, showing that local stimulation of the GSN optobody in a specifically targeted cell induced a spatially controlled defect in cell migration (Supplementary Fig. 16). This capability provides an opportunity for optically modulating endogenous GSN in a spatiotemporal manner.

Next, to examine the ability of β2AR optobody to inhibit endogenous β2AR, we photo-stimulated human embryonic kidney 293 (HEK293) cells expressing β2AR optobody and monitored downstream β2AR signaling[14]. Activation of β2AR with isoprenaline (ISO), resulting in β2AR internalization and cAMP-mediated Ca^{2+} influx, was blocked by the intact β2AR nanobody (Supplementary Figs. 17 and 18). In β2AR optobody-expressing cells, light illumination inhibited the internalization of β2AR-iRFP, significantly decreasing the relative internalization ratio to a degree comparable to that of the β2AR nanobody (Fig. 3d–f). The blue-light illumination of β2AR optobody-transfected cells also induced a decrease in Ca^{2+} influx into the cells, even with ISO treatment (Fig. 3g,h). These observations indicate that the activated β2AR optobody is capable of light-induced disruption of endogenous β2AR signaling.

In summary, we have developed an optogenetic platform, termed Optobody, for light-inducible regulation of intrabody activity and manipulation of endogenous target protein function. Although the representative intrabodies we developed showed a clear expression pattern in cells, intrabodies sometimes aggregate. Therefore, in choosing an intrabody as a backbone for optobody, it is important to consider the expression pattern of original intrabody inside cells. In addition, when some fragments of optobody such as C-terminal fragment of GFP optobody or N-terminal fragment of GCN4 optobody are highly expressed in cells, they have a self-aggregated tendency before stimulation (Supplementary Fig. 19). Even though the aggregation did not contain its target protein, it is another point to be considered in the use of optobodies in cellular applications.

In this study, we used blue-light responsive photoreceptors for generating optobodies. However, the concept underlying the optobody is a split intrabody fragment and reassembly via an inducer, and is thus not limited to blue-light stimulation. We strongly believe that our technique could be applied to other inducible dimerization systems, including a near-infrared induced optobody. Furthermore, there are a variety of techniques that use antibody fragments, such as chimeric antigen receptor-T (CAR-T) cells. The optobody might thus be applied to engineering of conventional antibody techniques to convert these tools to inducible antibody-activated systems, suggesting a broader drug-activating concept.

Online content

Any methods, additional references, Nature Research reporting summaries, source data, statements of code and data availability and associated accession codes are available at https://doi.org/10.1038/s41592-019-0592-7.

Received: 30 December 2018; Accepted: 6 September 2019;
Published online: 14 October 2019

References

1. Marschall, A. L., Dubel, S. & Boldicke, T. *MAbs* **7**, 1010–1035 (2015).
2. Miller, T. W. & Messer, A. *Mol. Ther.* **12**, 394–401 (2005).
3. Helma, J., Cardoso, M. C., Muyldermans, S. & Leonhardt, H. *J. Cell Biol.* **209**, 633–644 (2015).
4. Bethuyne, J. et al. *Nucleic Acids Res.* **42**, 12928–12938 (2014).
5. Tang, J. C. et al. *eLife* **5**, e15312 (2016).
6. Tischer, D. & Weiner, O. D. *Nat. Rev. Mol. Cell Biol.* **15**, 551–558 (2014).
7. Kirchhofer, A. et al. *Nat. Struct. Mol. Biol.* **17**, 133–138 (2010).
8. Kawano, F., Suzuki, H., Furuya, A. & Sato, M. *Nat. Commun.* **6**, 6256 (2015).
9. Proba, K., Honegger, A. & Pluckthun, A. *J. Mol. Biol.* **265**, 161–172 (1997).

10. Guntas, G. et al. *Proc. Natl Acad. Sci. USA* **112**, 112–117 (2015).
11. Caussinus, E., Kanca, O. & Affolter, M. *Nat. Struct. Mol. Biol.* **19**, 117–121 (2011).
12. Katoh, Y. et al. *J. Biol. Chem.* **291**, 10962–10975 (2016).
13. Panza, P., Maier, J., Schmees, C., Rothbauer, U. & Sollner, C. *Development* **142**, 1879–1884 (2015).
14. Staus, D. P. et al. *Mol. Pharm.* **85**, 472–481 (2014).
15. Van den Abbeele, A. et al. *Cell Mol. Life Sci.* **67**, 1519–1535 (2010).
16. Tanenbaum, M. E., Gilbert, L. A., Qi, L. S., Weissman, J. S. & Vale, R. D. *Cell* **159**, 635–646 (2014).

Acknowledgements

We thank J. Gettemans for kindly providing the GSN nanobody and S.-C. Kim for helpful discussions about intrabodies. We are grateful to N. Kim for statistical analysis and discussion, to J.-H. Kim and Y. Lee for experimental support and to S. Lee for discussions. This work was supported by a grant from the Institute for Basic Science (no. IBS-R001-G1), the National Research Fund (NRF-2018R1A2B3004764) and the KAIST Institute for the BioCentury, Republic of Korea.

Author contributions

D.Y., B.O.P. and W.D.H. conceived the idea and directed the work. D.Y., H.L., B.-H.O., B.O.P. and W.D.H. designed the experiments. D.Y., B.O.P., H.L., H.J. and J.H. performed the experiments. Y.J. created the custom MATLAB scripts. D.Y., H.L., B.O.P. and W.D.H. wrote the manuscript.

Competing interests

South Korean patent no. 10-2016-0013121 has been awarded to Institute for Basic Science (to D.Y., B.O.P. and W.D.H., being the inventors) for the optobody and chemobody technology described in this paper. The technology has been sold to Hulux and W.D.H. is a shareholder.

Additional information

Supplementary information is available for this paper at https://doi.org/10.1038/s41592-019-0592-7.

Correspondence and requests for materials should be addressed to B.O.P. or W.D.H.

Peer review information Rita Strack was the primary editor on this article and managed its editorial process and peer review in collaboration with the rest of the editorial team.

Methods

Plasmid construction. Individual optobody plasmids were generated using Gibson Assembly Cloning (NEB). All complementary DNA encoding optobody fragments were regulated by CMV promoter. Sequences encoding the GFP nanobody from pcDNA3_NSlmb-vhhGFP4 (Addgene, plasmid 35579) were used as a template for split GFP nanobody fragments. To create FRB–FKBP-conjugated split GFP nanobodies on a single expression plasmid, we first generated a vector containing FRB-mCherry-P2A-FKBP. Enhanced green fluorescent protain (EGFP) in pEGFP-C1 (Clontech) between *Age*I and *Bsp*EI sites was then replaced with PCR-amplified FRB-mCherry and P2A-FKBP sequences. Sequences of split GFP nanobody fragments (N-terminal fragments, residues 1–44, 1–65 and 1–90; C-terminal fragments, residues 45–117, 65–117 and 91–117) were PCR-amplified to contain glycine-serine linkers (GGGGS)x2 positioned immediately adjacent to the cleavage residue. PCR products encoding split GFP nanobody fragments and FRB-mCherry-P2A-FKBP were co-inserted into pEGFP-C1 (Clontech) after removing EGFP by digesting with *Afe*I and *Bsp*EI. nMagHigh1 and pMagHigh1, used for generating the GFP optobody, were synthesized by Cosmo Genetech. Sequences of the split GFP nanobody N-terminal fragment (residues 1–65) containing (GGGGS)x3 and nMagHigh1 were PCR-amplified and inserted into piRFP682-C1 at an *Eco*RI site. PCR-amplified sequences encoding the split GFP nanobody C-terminal fragment (residues 66–117) and pMagHigh1 (in different orientations) were cloned into pFusionRed-C1. The two sequences encoding the GFP nanobody C-terminal fragment and pMagHigh1 were connected by (GGGGS)x3 linkers. Expression plasmids for C24A and C24S mutant GFP nanobodies were generated by mutagenizing sequences encoding the N-terminal fragment of the GFP nanobody by PCR-driven overlap extension using mutagenic oligonucleotides. The resulting PCR-amplified sequences encoding mutant GFP nanobodies were inserted into pmCherry-N1 (Clontech). The C24S mutant GFP optobody was created by co-inserting PCR products encoding the C24S mutant GFP nanobody N-terminal fragment and nMagHigh1 into piRFP682-C1 at the *Eco*RI site. GFP optobody conjugated with the photoreceptor proteins, pMag and pMagFast1, were constructed by PCR-amplification followed by insertion with the GFP nanobody C-terminal fragment into pFusionRed-C1. PCR-amplified sequences encoding SspB (R73Q) or iLID were cloned into piRFP682-C1 or pFusionRed-C1 together with an N-terminal or C-terminal fragment of the GFP nanobody, respectively. The Tom20-GFP vector was constructed by excising a PCR product encoding Tom20 (residues 1–33) by digesting with *Eco*RI and *Bam*HI, followed by insertion into pEGFP-N1 (Clontech). Sequences encoding H2B, Giantin (residues 9391–9777) and KRAS tail (residues 502–561) were PCR-amplified and inserted into the pEGFP-C1 vector (Clontech) at *Eco*RI and B*am*HI sites.

The PA-deGraFP components NSlmb and NSnoFbox were generated using pcDNA3_NSlmb-vhhGFP4 (Addgene, plasmid 35579) and pcDNA3_NSnoFbox-vhhGFP4 (Addgene, plasmid 35580), respectively, as templates. PCR-amplified NSlmb-vhhGFP4 and NSnoFbox-vhhGFP4 were inserted into pFusionRed-N1 at *Nhe*I and *Eco*RI sites. PCR-amplified NSlmb was inserted into the previously generated GFP optobody vector containing an N-terminal or C-terminal fragment of the GFP nanobody at *Nhe*I/*Age*I and *Nhe*I/*Xho*I sites, respectively.

The protein sequences of the GFP nanobody, mCherry nanobody, actin nanobody, GSN nanobody, β2AR nanobody and scFvGCN4 VH domain were aligned using the T-Coffee Multiple sequence alignment program, and each split site of the intrabodies was selected. The actin optobody vector was constructed using an actin nanobody (Chromotek) as a template. PCR products encoding the actin nanobody N-terminal fragment (residues 1–64), C-terminal fragment (residues 65–168), (GGGGS)x3-nMagHigh1 and pMagHigh1-(GGGGS)x3 were PCR-amplified. The actin nanobody N-terminal fragment and (GGGGS)x3-nMagHigh1 pair was inserted into pmCherry-C1 (Clontech) at the *Age*I site, and the pMagHigh1-(GGGGS)x3 and C-terminal actin nanobody fragment pair was cloned into piRFP682-C1 at the *Bsp*EI site.

The mCherry optobody was generated by PCR-amplified sequences encoding the N-terminal fragment (residues 1–65) and C-terminal fragment (residues 66–129) of the mCherry nanobody. The amplified fragments were cloned with (GGGGS)x3-nMagHigh1 and pMagHigh1-(GGGGS)x3 into piRFP682-C1 and pmEGFP-N1, respectively, at the *Eco*RI site.

The GSN optobody was created by PCR-amplifying sequences encoding the N-terminal fragment (residues 1–65) and C-terminal fragment (residues 66–129) of the GSN nanobody (provided by J. Gettemans, Ghent University, Belgium). The resulting fragments were cloned together with (GGGGS)x3-nMagHigh1 and pMagHigh1-(GGGGS)x3 into pFusionRed-N1 and piRFP682-C1, respectively, at the *Eco*RI site. The FRB–FKBP-conjugated split GSN nanobody was generated according to the GSN optobody process by replacing the dimerization domains with FRB and FKBP. The C-terminal fragment of the split GSN nanobody was conjugated to mitochondria by inserting a PCR product encoding monoamine oxidase A (residues 490–527) into the ppMagHigh1-GSN nanobody C-terminal fragment-FusionRed and pFKBP-GSN nanobody C-terminal fragment-FusionRed at *Bsr*GI and *Not*I sites. The human GSN sequence was PCR-amplified from GSN-bio-His (Addgene, 52067) and inserted into pEGFP-C1 (Clontech) at the *Eco*RI site. The PCR-amplified sequence encoding GSN (G2–3) or GSN (G4–6) was also cloned into pEGFP-C1 (Clontech) at the *Eco*RI site.

scFvGCN4 sequences from pHRdSV40-scFv-GCN4-sfGFP-VP64-GB1-NLS (Addgene, plasmid 60904) were used as a template for the GCN4 optobody. The GCN4 optobody was generated by PCR-amplifying sequences encoding scFvGCN4 VL-VH N-terminal fragment (residues 1–196), scFvGCN4 VH C-terminal fragment (197–247), (GGGGS)x3-nMagHigh1 and pMagHigh1-(GGGGS)x3, and then cloning the scFvGCN4 VL-VH N-terminal fragment-(GGGGS)x3-nMagHigh1 and pMagHigh1-(GGGGS)x3-scFvGCN4 VH C-terminal fragment into pFusionRed-N1 and piRFP682-C1, respectively, at the *Eco*RI site. In the case of splitting the VL domain of scFvGCN4, sequences encoding the scFvGCN4 VL N-terminal fragment (residues 1–64) and scFvGCN4 VL C-terminal-VH fragment (residues 65–247) were PCR-amplified and cloned as described for the GCN4 optobody cloning process. scFvGCN4 VH conjugated with (GGGGS)x3-nMagHigh1 and scFvGCN4 VL conjugated with pMagHigh1-(GGGGS)x3 also were generated in the same manner. A vector encoding Mito-conjugated 24xGCN4 peptides was created from pcDNA4TO-Mito-mCherry-24xGCN4_v1 (Addgene, plasmid 60913) by replacing mCherry with EGFP at *Eco*RI and *Not*I sites.

The β2AR optobody was generated from the β2AR nanobody (synthesized by Genescript) and PCR-amplified sequences encoding N-terminal (residues 1–65) and C-terminal (residues 66–117) fragments of the β2AR nanobody. The resulting fragments were PCR-amplified together with (GGGGS)x3-nMagHigh1 and pMagHigh1-(GGGGS)x3, respectively. A single vector expressing β2AR optobody was generated by connecting the β2AR nanobody N-terminal fragment-(GGGGS)x3-nMagHigh1 and pMagHigh1-(GGGGS)x3- β2AR nanobody C-terminal fragment with a tension linker and inserting the resulting product into pFusionRed-N1 at *Age*I and *Bam*HI sites. The β2AR-iRFP682 expression vector was created by cloning cDNA encoding human β2AR into piRFP682-N1 at the *Eco*RI site. A plasmid encoding Cnga2(C460W/E583M)-EGFP was constructed by inserting cDNA encoding mouse Cnga2 into pEGFP-N1 at the *Eco*RI site. PCR-amplified Cnga2 containing a C460W mutation was cloned, after which a Cnga2 sequence containing C460W and E583M mutations was cloned into pEGFP-C1 at the *Eco*RI site.

Cell culture and transfection. HeLa, NIH3T3 and HEK293 (ATCC) cells were maintained in Dulbecco's Modified Eagle's Medium (Gibco) supplemented with 10% fetal bovine serum (Invitrogen) at 37 °C in a humidified 10% CO_2 atmosphere. Cells were tested using an e-Myco Mycoplasma PCR detection kit (iNtRON) and confirmed to be free from mycoplasma.

cDNA encoding each optobody N-terminal and C-terminal fragment was transfected at a 1:1 ratio. For monitoring migration of NIH3T3 cells, NIH3T3 cells were plated on a 96-well plate pre-coated with 5 μg ml^{-1} fibronectin. For imaging, HEK293 cells were plated on a 96-well plate pre-coated with poly-D-lysine and then transfected using either a jetPrime (Polyplus) or Microporator (Neon Transfection System, Invitrogen), according to the manufacturers' instructions. Electroporation conditions were additionally optimized to increase transfection efficiency for HeLa cells (two pulses of 980 V for 35 ms) and NIH3T3 cells (three pulses of 1,450 V for 10 ms).

Protein production of recombinant GFP and anti-GFP nanobody variants. DNA fragments encoding EGFP was inserted to pJAhX vector plasmid (home-made) to obtain the protein fused to a poly-histidine (His_{10}) tag at its N terminus. The modified plasmid was transformed into *Escherichia coli* BL21(DE3) RIPL strain (Novagen). Expression of the protein was induced by the addition of 0.1 mM isopropyl-β-D-thio-galactoside (IPTG) at 18 °C when the bacteria grew to an optical density (OD_{600}) of 0.6 in LB medium. Bacterial cell lysate with overexpressed His_{10}-EGFP was prepared by sonication in Buffer A (20 mM Tris-HCl pH 7.5, 100 mM NaCl and 1 mM NaN_3). The supernatants of each sample were applied to gravity flow columns filled with HisPur cobalt resin (Thermo Scientific). Resin-bound His_{10}-EGFP was washed with 3 column volumes of 10 mM imidazole-added Buffer A, and eluted with 200 mM imidazole-added Buffer A. Eluted sample was further purified with a HiTrapQ HP anion exchange column (GE Healthcare). For size-exclusion chromatography, the unbound fractions from HiTrapQ HP were collected and loaded onto a HiLoad 26/60 Superdex 75 gel filtration column (GE Healthcare). Purified His_{10}-EGFP was concentrated by using an Amicon Ultra 10K (Millipore).

PCR products of GFP nanobody, GFP nanobody N65-FRB and FKBP-GFP nanobody C66 were individually inserted into pJKXCPDh plasmids (home-made) to express proteins fused to His_{10}-tagged CPD (cysteine protease domain) at their C terminus. The strain, culture condition and induction condition of *E. coli* were same in the case of EGFP. Bacterial cell lysate with overexpressed GFP nanobody, GFP nanobody N65-FRB or FKBP-GFP nanobody C66 were individually prepared by sonication in Buffer A. The supernatants of each sample were applied to gravity flow columns filled with HisPur cobalt resin (Thermo Scientific). To remove the CPD-His_{10} tag and elute the protein from cobalt resin, resin-bound GFP nanobody, GFP nanobody N65-FRB and FKBP-GFP nanobody C66 were treated with Buffer A containing 0.1 mM phytate for 2 h and eluted. Further purification and concentration steps were same in the case of EGFP.

To obtain rapamycin-engaged GFP nanobody N65-FRB and FKBP-GFP nanobody C66 heterodimer, the PCR product of GFP nanobody N65-FRB was inserted into pJAX vector (home-made). The modified plasmid was co-transformed with FKBP-GFP nanobody C66 pJKXCPDh into BL21(DE3) RIPL.

Expression of the protein was induced by the addition of 0.1 mM IPTG at 18 °C when the bacteria grow to an OD_{600} of 0.6 in LB. At the same time, 10 μM of rapamycin was also treated to induce FKBP–FRB dimerization. The protein purification and concentration steps were same in the case of GFP nanobody N65-FRB or FKBP-GFP nanobody C66.

BLI measurement. To obtain kinetic parameters of protein–protein interaction including a K_D value of EGFP and GFP nanobody, BLI measurement was performed using the BLItz instrument (ForteBio). A 4 μl volume of His_{10}-EGFP (4 mg ml^{-1}) was loaded onto a nickel-nitrilotriacetic acid (Ni-NTA) biosensor for 120 s. The baseline was determined by incubating the sensor with 400 μl Buffer A for 30 s. To measure protein association until reaching a steady state, 4 μl volume of GFP nanobody was used. The binding was used to measure protein dissociation (for a duration of 180 s). After repeated BLI measurements in more than three different concentrations of GFP nanobody, the binding kinetics between EGFP and GFP nanobodies was deduced by using BLItz Pro software (ForteBio). Binding kinetics between EGFP and GFP nanobody N65-FRB, FKBP-GFP nanobody C66 or rapamycin-engaged GFP nanobody N65-FRB, FKBP-GFP nanobody C66 were measured using the same process as for the GFP nanobody. Additional data from the process is provided in Supplementary Note 1.

Co-immunoprecipitation assay and western blot. Hela cells were transfected with sequence motif DYKDDDDK (FLAG)-GFP nanobody-iRFP, FLAG-iRFP-GFP nanobody N65-nMagHigh1, FLAG-pMagHigh1-GFP nanobody C66-FuRed or both FLAG-iRFP-GFP nanobody N65-nMagHigh1 and Myc-pMagHigh1-GFP nanobody C66-FuRed with human influenza hemagglutinin (HA)-tagged GFP by using jetPrime (Polyplus). At 4 h after transfection, cells were illuminated with blue LEDs (Photron) for 24 h. Cells were collected and cell extracts were prepared with Pierce immunoprecipitation lysis buffer (Thermo Scientific) containing Halt protease inhibitor cocktail (Thermo Scientific). Lysates were incubated with Monoclonal anti-FLAG M2 antibody (Sigma) overnight at 4 °C on a rocking platform. Protein A/G PLUS-Agarose (Santa Cruz) was added to the mixture for 2 h at 4 °C while rotating. And then the beads were collected by centrifugation, washed in lysis buffer and resuspended in SDS gel loading buffer. The proteins were separated on Bolt 4–12% Bis-Tris Plus Gels, transferred to a polyvinylidene difluoride membrane using iBlot Transfer Stack (Gibco) and detected by immunoblotting.

Membranes were blocked with TBS/Odyssey blocking buffer and stained with Rabbit anti-HA (Cell Signaling), Rabbit anti-FLAG (Cell signaling), Rabbit anti-Myc (Abcam) and Mouse anti-GAPDH (Thermo Scientific) overnight at 4 °C with shaking. After washing with TBST three times, the membranes were stained with IRDye 680RD Goat anti-Rabbit immunoglobulin G (IgG) (heavy + light chains; H+L) and IRDye 800CW Goat anti-Mouse IgG (H+L) (LI-COR) for 1 h at room temperature. After washing with TBST three times, the membrane were imaged with LI-COR Odyssey using the Image Studio software.

Live-cell imaging and photoactivation. For imaging, all cells were plated on 96-well plates (μ-Plate 96-well ibiTreat, ibidi GmbH). Live-cell imaging was performed using a Nikon A1R confocal microscope (Nikon Instruments) mounted onto a Nikon Eclipse Ti body equipped with a Nikon CFI Plan Apochromat VC objective (×60/1.4 numerical aperture, Nikon Instruments) and an ImageXpress Micro XLS automated epifluorescence microscope (Molecular Devices) equipped with a ×10 Plan Fluor objective and a 4.66 megapixel CMOS camera with a 16-bit readout. A Chamlide TC system placed on a Nikon A2R confocal microscope stage was used for maintaining environmental conditions at 37 °C and 10% CO_2 (Live Cell Instruments).

For cells imaged using the Nikon A1R confocal microscope (Nikon Instruments), photoactivation was conducted using a 488-nm laser emitted through a Galvano scanner, incorporated in a hybrid confocal scan head with a high-speed hyper selector (Nikon). The shape and size of the photoactivated region were adjusted using Nikon imaging software (NIS-elements). A laser power density of 490 μW mm^{-2} (measured with an ADCMT optical power meter) was used for photoexcitation. Photoactivation was also delivered with 96 blue LEDs (Photron) mounted on a customized array (Live Cell Instruments) that provided a peak emission of 470 nm with 250 μW mm^{-2} (measured with an ADCMT optical power meter). For imaging cells on the ImageXpress Micro XLS automated epifluorescence microscope (Molecular Devices), the excitation light was produced with an excitation filter for GFP (GFP-3035D-NTE-ZERO, Semrock). A light intensity of 40 μW mm^{-2} was used for photoactivation.

Image processing and analysis. Images were analyzed using Nikon imaging software (NIS-elements AR 64-bit v.3.21, Laboratory Imaging), ImageJ software (v.1.50b, US National Institutes of Health; http://imagej.nih.gov/ij/), or MATLAB software (v.R2015a, Mathworks). Colocalization of two molecules in different fluorescence colors was quantitatively analyzed with Pearson's correlation coefficient using custom MATLAB scripts (available in the Supplementary Code file). The intensity pattern along a line was measured with the Plot Profile tool in ImageJ software. The degradation of EGFP-H2B and changes in the fluorescence intensity of R-GECO were analyzed by measuring fluorescence intensity at designated regions of interest using the Annotations and Measurements tool or Time Measurement tool. Cell migration tracking data were produced using the MTrackJ plugin in ImageJ software, and analyzed using programs described in the protocol[17]. Migration tracks were displayed using the Plot_At_Origin program. Migration distance and instantaneous speed were calculated using the Speed program. For analysis of β2AR internalization, the shape of the entire cell and internalized portion were drawn using Polygon selection in ImageJ software. The fluorescence intensity of the selected region was recorded using the ROI manager in ImageJ software, and internalized receptors were calculated through inside fluorescence intensity/total fluorescence intensity[18]. Statistical significance was evaluated using a two-tailed Student's *t*-test.

Statistics and reproducibility. The experiments in Figs. 1b,f,g, 2a–c,e–g and 3a–h, Supplementary Figs. 1d,e, 3b,c, 5a–d, 6a–d, 7a,b,d,e, 8b–d, 9c ,d, 10a–d, 11a–d, 12a–e, 13a–c, 14b–e, 15a–c, 16a–d, 17a–d, 18a–c and 19a–d and Supplementary Videos 1–7 were repeated with multiple independent experiments (at least three times) originating from independent cell culture. Each experiment produced similar results. The affinity in Supplementary Fig. 3 were once measured with the purified protein in one experiment. The detailed value of BLI results is provided in Supplementary Note 1. The co-immunoprecipitation assay in Supplementary Fig. 4 was performed four times originating from independent cell preparation, resulting in similar data to the western blot.

The *n* value in figure legends represents the number of cells imaged per condition. For quantification and statistical significance test, data is displayed as combined graphs from multiple experiments and applied by a two-tailed Student's *t*-test. Before the Student's *t*-test, an *F*-test was performed to compare variances.

The statistical information for each figure is described below.

Figure 1b from top to bottom: $n=8$, split site 44/45; $n=8$, split site 65/66; $n=10$, split site 90/91; *P* values: split site 44/45 versus 65/66 at +Rap, $P=4.58\times10^{-5}$; split site 65/66 versus 90/91 at +Rap, $P=7.06\times10^{-4}$ by Student's two-tailed *t*-test.

Figure 3b,c: FuRed, $n=205$; GSN nanobody, $n=132$; GSN optobody, $n=136$. Figure 3b: *P* values: FuRed versus GSN optobody at 0 h, $P=0.0538$; GSN nanobody versus GSN optobody at 2 h, $P=0.0035$ by Student's two-tailed *t*-test. Figure 3c: *P* values: GSN optobody −Light versus +Light, $P=7.89\times10^{-4}$; GSN nanobody versus GSN optobody at +Light, $P=0.8994$ by Student's two-tailed *t*-test.

Figure 3e,f: $n=37$, FuRed; $n=23$, β2AR nanobody; $n=44$, β2AR nanobody –Light; $n=37$, β2AR nanobody +Light. Figure 3e: *P* values: β2AR nanobody –Light versus +Light, $P=0.0571$ by Student's two-tailed *t*-test. Figure 3f: *P* values: β2AR nanobody versus β2AR optobody, $P=0.6046$; β2AR nanobody –Light versus +Light, $P=8.62\times10^{-9}$ by Student's two-tailed *t*-test.

Figure 3h: $n=67$, iRFP; $n=51$, β2AR nanobody; $n=62$, β2AR nanobody –Light; $n=50$, β2AR nanobody +Light; *P* values: β2AR nanobody –Light versus +Light, $P=6.06\times10^{-5}$ by Student's two-tailed *t*-test

Reporting Summary. Further information on research design is available in the Nature Research Reporting Summary linked to this article.

Data availability

The data supporting the findings of this study are available within the paper and its Supplementary Information files. Extra data are available from the corresponding author upon reasonable request.

Code availability

The code for high-throughput analysis of two-channel time-lapse colocalization in individual cells are available in Supplementary code files.

References

17. Gorelik, R. & Gautreau, A. *Nat. Protoc.* **9**, 1931–1943 (2014).
18. Siuda, E. R. et al. *Nat. Commun.* **6**, 8480 (2015).

nature research

Corresponding author(s): Won Do Heo

Last updated by author(s): Aug 20, 2019

Reporting Summary

Nature Research wishes to improve the reproducibility of the work that we publish. This form provides structure for consistency and transparency in reporting. For further information on Nature Research policies, see Authors & Referees and the Editorial Policy Checklist.

Statistics

For all statistical analyses, confirm that the following items are present in the figure legend, table legend, main text, or Methods section.

n/a	Confirmed	
☐	☒	The exact sample size (*n*) for each experimental group/condition, given as a discrete number and unit of measurement
☐	☒	A statement on whether measurements were taken from distinct samples or whether the same sample was measured repeatedly
☐	☒	The statistical test(s) used AND whether they are one- or two-sided *Only common tests should be described solely by name; describe more complex techniques in the Methods section.*
☒	☐	A description of all covariates tested
☒	☐	A description of any assumptions or corrections, such as tests of normality and adjustment for multiple comparisons
☐	☒	A full description of the statistical parameters including central tendency (e.g. means) or other basic estimates (e.g. regression coefficient) AND variation (e.g. standard deviation) or associated estimates of uncertainty (e.g. confidence intervals)
☐	☒	For null hypothesis testing, the test statistic (e.g. *F*, *t*, *r*) with confidence intervals, effect sizes, degrees of freedom and *P* value noted *Give P values as exact values whenever suitable.*
☒	☐	For Bayesian analysis, information on the choice of priors and Markov chain Monte Carlo settings
☒	☐	For hierarchical and complex designs, identification of the appropriate level for tests and full reporting of outcomes
☐	☒	Estimates of effect sizes (e.g. Cohen's *d*, Pearson's *r*), indicating how they were calculated

Our web collection on statistics for biologists contains articles on many of the points above.

Software and code

Policy information about availability of computer code

Data collection	Data was collected by Nikon imaging software (NIS-elements AR 64-bit v 3.21, Laboratory Imaging), MetaMorph software (v 7.8.12, MDS Analytical Technologies) and Odyssey CLx software (Image Studio v3, LI-COR Biosciences).
Data analysis	Imaging data was analyzed in Nikon imaging software 3.21, ImageJ software 1.50b or Matlab R2015a. Scripts were written in Matlab R2015a. Data was analyzed in Graphpad Prism 6 and Microsoft Excel.

For manuscripts utilizing custom algorithms or software that are central to the research but not yet described in published literature, software must be made available to editors/reviewers. We strongly encourage code deposition in a community repository (e.g. GitHub). See the Nature Research guidelines for submitting code & software for further information.

Data

Policy information about availability of data

All manuscripts must include a data availability statement. This statement should provide the following information, where applicable:

- Accession codes, unique identifiers, or web links for publicly available datasets
- A list of figures that have associated raw data
- A description of any restrictions on data availability

Supporting data of this study are available from the corresponding author on reasonable request.

Field-specific reporting

Please select the one below that is the best fit for your research. If you are not sure, read the appropriate sections before making your selection.

☒ Life sciences ☐ Behavioural & social sciences ☐ Ecological, evolutionary & environmental sciences

Life sciences study design

All studies must disclose on these points even when the disclosure is negative.

Sample size	No statistical method was used to pre-determine sample size. The detailed information was provided in the figure legend.
Data exclusions	No data were excluded.
Replication	At least 3 independent cell preparations were performed for most cases, as noted in the figure legend. All attempts at replications were successful.
Randomization	This is not relevant to cell biology studies and samples were not randomized.
Blinding	This is not relevant to cell biology studies and samples were not blinded

Reporting for specific materials, systems and methods

We require information from authors about some types of materials, experimental systems and methods used in many studies. Here, indicate whether each material, system or method listed is relevant to your study. If you are not sure if a list item applies to your research, read the appropriate section before selecting a response.

Materials & experimental systems

n/a	Involved in the study
☐	☒ Antibodies
☐	☒ Eukaryotic cell lines
☒	☐ Palaeontology
☒	☐ Animals and other organisms
☒	☐ Human research participants
☒	☐ Clinical data

Methods

n/a	Involved in the study
☒	☐ ChIP-seq
☒	☐ Flow cytometry
☒	☐ MRI-based neuroimaging

Antibodies

Antibodies used	Monoclonal ANTI-FLAG M2 antibody (Sigma, F1804) Antibody name (manufacturer, Cat. no., Dilution) Rabbit anti-HA (Cell Signaling, 3724, 1:1000), Rabbit anti-FLAG (Cell signaling, 14793, 1:1000), Rabbit anti-Myc (Abcam, ab9106, 1:1000), Mouse anti-GAPDH (Thermo Scientific, MA5-15738, 1:3000), IRDye 680RD Goat anti-Rabbit IgG (H+L) (LI-COR, 926-68071, 1:3000), IRDye 800CW Goat anti-Mouse IgG (H+L) (LI-COR, 926-32210, 1:3000)
Validation	Monoclonal ANTI-FLAG M2 antibody: Specific for DYKDDDDK protein sequence. Validated for immunocytochemistry from manufacturer Rabbit anti-HA: Specific for YPYDVPDYA protein sequence. Validated for western blot from manufacturer Rabbit anti-FLAG: Specific for DYKDDDDK protein sequence. Validated for western blot from manufacturer Rabbit anti-Myc: Specific for EQKLISEELD protein sequence. Validated for western blot from manufacturer Mouse anti-GAPDH: Specific for GAPDH. Validated for western blot from manufacturer Anti-FLAGs, anti-HA and anti-Myc have been additionally validated for immunocytochemistry by overexpressing FLAG, HA or Myc-tagged protein, respectively, at HeLa cell.

Eukaryotic cell lines

Policy information about cell lines

Cell line source(s)	Hela, NIH3T3 and HEK293 cell lines were acquired from ATCC.
Authentication	No additional authentication was performed for cells purchased in ATCC. ATCC authenticates cell lines using STR analysis according to the product specification webpage.
Mycoplasma contamination	All cell lines were confirmed negative for mycoplasma contamination.

Commonly misidentified lines (See ICLAC register)	No commonly misidentified cell lines were used.